

Hydrogen Self Shielding in a Quasar Proximity Zone

Gabriel Altay¹, Rupert A. C. Croft¹, and Tiziana Di Matteo¹,

¹ *McWilliams Center for Cosmology, Carnegie Mellon University*

Accepted 200? ???? ?. Received 2009 ???? ??. in original form 2009 xx

ABSTRACT

We calculate the distribution of neutral Hydrogen within 750 proper $h^{-1}\text{kpc}$ of a quasar, $L_{\text{bol}} = 1.62 \times 10^{13} L_{\odot} \approx L_{\text{Edd}}$, powered by accretion onto a super massive black hole, $M_{\text{BH}} = 4.47 \times 10^8 M_{\odot}$, at $z = 3$. Our numerical model includes cosmological initial conditions, gas dynamics, star formation, supernovae feedback, and the self consistent growth and thermal feedback of black holes calculated using GADGET as well as a detailed post-processing ray tracing treatment of the non-uniform ionizing radiation field calculated using SPHRAY. Our radiative transfer scheme naturally accounts for the self shielding of optically thick systems near the luminous central source. We show that the correct treatment of self shielding introduces a flattening feature into the neutral column density distribution around $\text{Log } N_{\text{HI}} = 20$ and that regions with the lowest neutral fractions are not necessarily those with the highest density gas.

For comparison with our numerical work, we solve a Ricatti equation which determines the equilibrium Hydrogen ionization fractions in the presence of a radiation field that falls off as one over r squared with regions above a given gas density threshold completely shielded from ionizing radiation. We demonstrate that these simple semi analytic models cannot reproduce the neutral Hydrogen field calculated using SPHRAY. We conclude by comparing our models of this single proximity zone to observations by Hennawi and Prochaska of the absorption spectra of background quasars which are coincident on the sky with foreground quasars in their Quasars Probing Quasars (QPQ) series of papers. Compared to the QPQ sample, we find a factor of 3 fewer optically thick ($\text{Log } N_{\text{HI}} \geq 17.2$) systems around our quasar, however the dark matter halo that hosts our simulated quasar, $M_{\text{Halo}} = 5.25 \times 10^{12} M_{\odot}$, is less massive than the typical QPQ host halo by a factor of four. Allowing for a linear scaling between halo mass, baryonic overdensity and number of absorbers, we estimate the typical host halo mass in the QPQ sample as $1.92 \times 10^{13} M_{\odot}$.

Key words: astrophysics, theory, numerical, simulation, SPH, ray tracing, simulation, radiative transfer, quasar, AGN, black hole

1 INTRODUCTION

After the reionization of the Universe by the first luminous objects, the majority of neutral Hydrogen resides in gravitationally collapsed objects, specifically Damped Lyman- α systems (DLAs). These systems are observed via absorption lines in the spectra of distant quasars and are historically identified as those absorbers with HI column densities $N_{\text{HI}} > 2 \times 10^{20} \text{cm}^{-2}$ with lower column density systems $10^{17.2} < N_{\text{HI}} < 2 \times 10^{20} \text{cm}^{-2}$ being labeled Lyman Limit Systems (LLSs, see Wolfe et al. 2005, for a review). In contrast, the systems that give rise to the Lyman- α forest have $N_{\text{HI}} < 10^{17.2} \text{cm}^{-2}$ (see Rauch 1998; Weinberg et al. 2003, for reviews). This historical column density threshold ($N_{\text{HI}} = 10^{17.2} \text{cm}^{-2}$) serves to divide systems into those

that are predominantly neutral (the DLAs and LLSs) and those that reside in the mostly ionized intergalactic medium (IGM). The DLAs and LLSs remain mostly neutral in the presence of an ionizing ultraviolet (UV) background and local point sources through self shielding. Studying them in absorption opens a window into the post reionization population of cold, dense, neutral gas and provides a survey technique with a bias complimentary to that of emission surveys.

To study these systems numerically requires treating the UV ionizing background at some level. Many cosmological simulations have followed in the steps of Haardt & Madau (1996) and Katz et al. (1996a) by considering a spatially uniform, time variable, background with a spectral shape characteristic of quasar and stellar radia-

tion that has been reprocessed by the IGM. The background plays a role in determining the cooling function of cosmological gas and so its inclusion is also necessary at some level for a realistic description of galaxy and star formation. A uniform background is a good first approximation if one is interested in radiative cooling, however it ignores completely the self shielding that defines the DLAs and LLSs.

The most straight forward way to account for this shielding is to reduce the UV field to zero in regions above a given gas density threshold as was done in Haehnelt et al. (1998). A more detailed treatment based on the solution for plane parallel radiation incident on a constant density slab is described in Katz et al. (1996b) and used in the work of Gardner et al. (1997a, 2001, 1997b). These corrections are not based on transferring radiation through the simulation volume, but rather on applying the plane parallel solution on a pixel by pixel basis to HI column density maps in post processing.

Other approaches to self shielding include that of Cen et al. (2003) who include attenuation of the UV background on a cell by cell basis akin to Katz et al. (1996b). Razoumov et al. (2006), who include a treatment of the transfer of ionizing radiation in post processing using the Fully Threaded Transport Engine (FTTE) described in Razoumov & Cardall (2005). And Nagamine et al. (2007), who use a multi phase gas model to treat star formation and assume the cold dense phase to be fully neutral.

Recently, a series of nested galaxy formation simulations at different resolutions was used by Pontzen et al. (2008) to study DLAs over a broad range of mass scales. They include a simplified radiative transfer scheme to account for self shielding which lies somewhere between the full radiative transfer modeling and the pixel by pixel corrections.

The works mentioned above were aimed at studying systems where the radiation field is not dominated by a local point source. Miralda-Escudé (2005) applied simple analytic arguments based on the conservation of surface brightness to argue that *on average* the effect from local sources is negligible compared to that of the background for systems with optical depths below that of Lyman Limit Systems. On the other hand, Schaye (2006) use analytic arguments to show the local radiation field is likely to be important for denser systems that tend to cluster around the large scale overdensities that host these sources.

In this work, we examine the balance between the UV background, local sources, and self shielding by combining, for the first time, a hydrodynamic simulation that tracks the formation and accretion history of black holes with a detailed ray tracing treatment of the non-uniform UV radiation field. Shielding is most important in the presence of dense gas and strong UV fields, both of which occur near active galactic nuclei (AGN) and quasars. In fact, the transition between the background UV field and the local AGN/quasar UV field serves to define the proximity region of these objects. With the availability of large quasar catalogues and high resolution spectroscopy, it has become possible to study absorbers proximate to a foreground quasar in the spectrum of a coincident background quasar. Work such as this has been carried out in a series of papers entitled “Quasars Probing Quasars”, the first of which is authored by Hennawi et al. (2006) (HP06 in the rest of this paper). We compare our numerical models to observations from this

body of work and to theoretical calculations of the HI column density by Zheng & Miralda-Escudé (2002).

The format of this paper is as follows. In §2 we describe the GADGET simulation that determines our temperature and density fields, in §3 we review the ray tracing code SPHRAY used to calculate the transfer of ionizing radiation through this density field, in §4 we describe how we model our sources of ionizing radiation, in §5 we describe our semi analytic model, in §6 we describe our ray tracing results and compare them to the semi analytic model, in §7 we compare our theoretical results with those of Hennawi et al. (2006), and Zheng & Miralda-Escudé (2002) and in §8 we conclude and discuss further work.

2 COSMOLOGICAL HYDRODYNAMIC SIMULATION

The proximity zone we study in this work was cut from a cosmological simulation performed using a modified version of the publicly available Smoothed Particle Hydrodynamics (SPH) code GADGET (Springel 2005). The interested reader is directed to Di Matteo et al. (2008) for a full description of the simulation, however we will briefly describe it here.

We have adopted cosmological parameters consistent with the WMAP first year results (Spergel et al. 2003), specifically $(H_0, \Omega_m, \Omega_\Lambda, \Omega_b, \sigma_8) = (70, 0.3, 0.7, 0.04, 0.9)$, where H_0 is the Hubble parameter today, Ω_m , Ω_Λ , and Ω_b are the total matter, dark energy, and baryonic matter density parameters, and σ_8 is the mass variance in spheres of $8 h^{-1} \text{Mpc}$. The simulation volume is a periodic cube of side length $33.75 \text{ comoving } h^{-1} \text{Mpc}$. The matter distribution is sampled initially¹ by 486^3 dark matter and 486^3 baryonic particles, resulting in a mass per particle of $2.41 \times 10^7 h^{-1} \text{M}_\odot$ for the dark matter and $3.72 \times 10^6 h^{-1} \text{M}_\odot$ for the baryons. The simulation was evolved from redshift $z = 99$ to $z = 1$, and we centered our cutout on the most luminous accreting black hole from a snapshot at $z = 3$ near the peak of quasar activity.

The main physics elements of the simulation include a Tree-PM solver for gravity (e.g. Bagla 2002), an entropy conserving implementation of SPH for hydrodynamics from Springel & Hernquist (2002), a model for star formation and feedback by supernovae described in Springel & Hernquist (2003), optically thin radiative cooling in the presence of a spatially uniform UV background as in Katz et al. (1996a), and a model for the accretion of gas onto black holes and the associated thermal feedback described in Di Matteo et al. (2005) and Springel et al. (2005).

This GADGET simulation provides the base density and temperature fields for our work. In Figure 1, we show their distribution. The red grouping in the lower left corner of each panel represents the underdense to mildly overdense intergalactic medium (IGM) responsible for the Lyman α forest. Its slope determines the effective equation of state of the IGM. The green/yellow grouping above that is the

¹ During the course of the simulation, baryonic particles can lose mass by spawning stellar particles and can disappear all together through accretion onto black hole sink particles.

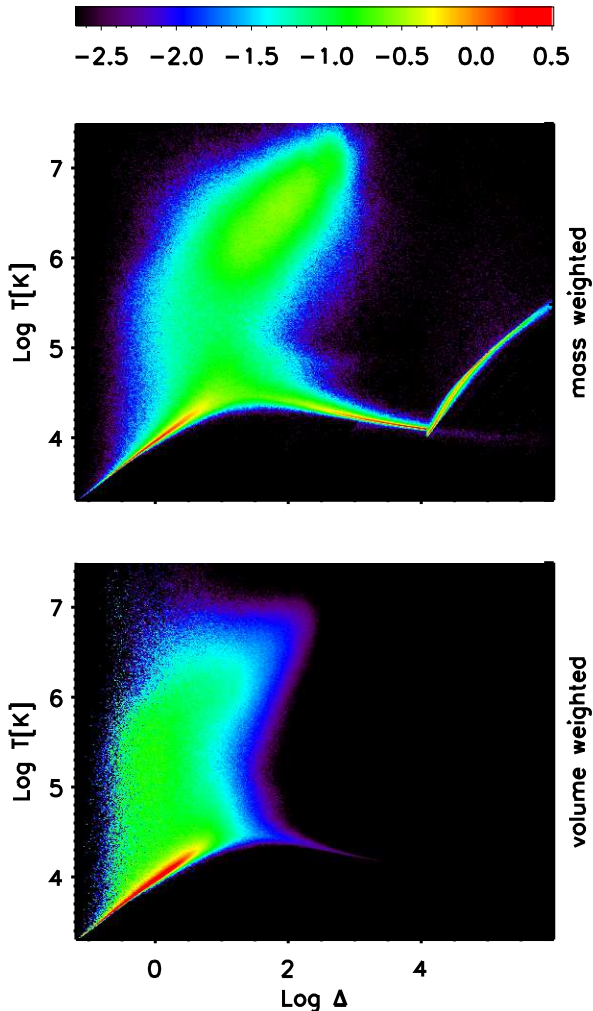


Figure 1. Density vs Temperature distribution. These quantities are fixed across all radiative models. Shown in the top (bottom) panel is the mass (volume) weighted probability density distribution in $\text{Log } \Delta - T$ space where Δ is the gas density in units of the baryon critical density and T is the temperature in Kelvin [i.e. an integral over the plane shown will give unity]. The color bar is logarithmic such that a unit difference between two pixels indicates a factor of ten difference in mass (volume).

warm/hot intergalactic medium. The check mark shaped region above $\Delta \approx 1000$ in the mass weighted panel represents collapsed objects where the bulk of neutral Hydrogen resides.

3 RADIATIVE TRANSFER SIMULATIONS

The thermal state of the gas in the hydrodynamic GADGET simulation described above is set by photo heating from a uniform UV background, shock heating, cosmic expansion, and direct energy injection due to feedback from supernovae and accreting black holes. The ionization state is set by assuming photo ionization equilibrium with the uniform UV background, and taking account of the temperature dependent collisional ionization and recombination rates. We wish

to improve the treatment of the UV field while preserving the local thermal feedback effects from supernovae and black holes. To do this, we select the black hole with the largest accretion rate from a GADGET snapshot at $z = 3$, cut out a $6 h^{-1} \text{Mpc}$ (comoving) region centered on it, and fix the density and temperature fields. We then calculate the equilibrium ionization state of the gas in the presence of a non uniform ionizing radiation field. To do this, we use two methods. The first is a semi analytic model which includes a self shielding gas density threshold above which the photoionization rate is set to zero. The second is a detailed ray tracing calculation of the non uniform UV radiation field which naturally accounts for self shielding. This ray tracing is accomplished with SPHRAY.

A detailed description of the code can be found in Altay et al. (2008), however we will outline the important features here. SPHRAY is a long characteristics, monte carlo, ray tracer for radiative transfer post processing. It works by transporting a large number of photon packets through the smoothing kernels of an SPH density field. The origin, direction, and frequency of each packet is sampled from user supplied probability distribution functions. It does not require that the SPH density field be smoothed and so can preserve its Lagrangian and adaptive nature. For this project, it was necessary to update the ionization solver to handle the very small neutral fractions (on the order of 10^{-8}).

For all of the radiative transfer (RT) calculations in this paper, the Hydrogen ionization fractions and temperatures of all particles are initialized to the values in the GADGET snapshot. The density field is then exposed to one of several non uniform radiation fields (see §4) until it reaches an equilibrium state. In the following sections, we make comparisons between the neutral density fields produced using SPHRAY and the semi analytic model.

We are justified in calculating the equilibrium neutral fractions by the fact that at $z = 3$ we are not calculating the expansion of an ionization front but the response of the gas to an inhomogeneous radiation field that has been in place long enough for the gas to respond. The light crossing time from the central quasar to the corner of the simulation volume is $\approx 6 \text{ Myr}$. This means that light travel times will have to be taken into account if we want to consider variable luminosities on time scales shorter than this. For the current work we assume the central point source has had a steady luminosity long enough for the influence of this source to propagate to the whole cut out and for the gas in the cut out region to respond to this radiation field.

We have used the case A recombination rates as most of the photons emitted by the recombining gas will leave the highly ionized computational volume. This is not the correct approximation for the self shielded gas, however the very small ionization fractions in these collapsed objects imply that only a small fraction of the gas there is actually recombining.

4 SOURCES OF IONIZING RADIATION

In this section we describe our various source models. We decompose the radiation field into components due to the UV background which comes into the simulation volume from the boundaries, the central quasar, the smaller satel-

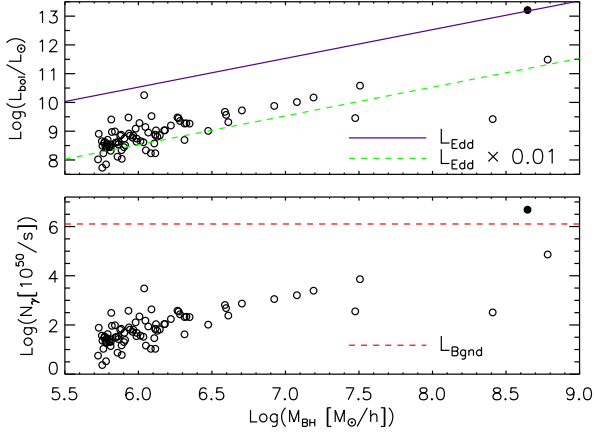


Figure 2. Luminosity of the accreting black holes contained within our cutout volume vs their mass. The bottom panel shows the number of Hydrogen ionizing photons emitted per second assuming a spectral slope of $\alpha_{\text{UV}} = 1.76$. This plot takes into account bolometric corrections. Also shown in the bottom panel (dotted line) is the contribution from the background UV field. The top panel shows the bolometric luminosity of each black hole and lines indicating the Eddington luminosity, L_{Edd} , and one hundredth L_{Edd} . The central quasar in our cutout region (the most luminous source) is the filled circle in both panels.

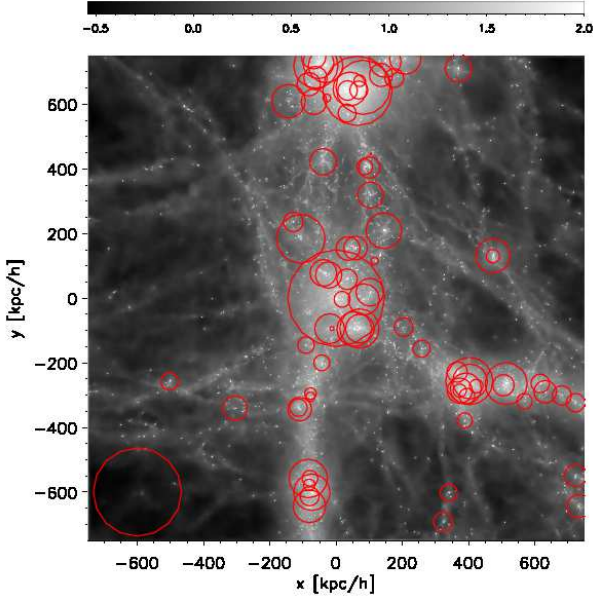


Figure 3. Projection of the gas density and source positions in the cutout region onto the x-y plane. The image was made by collapsing the $750^3 h^{-3} \text{kpc}^3$ volume along the z-axis. Shown in black and white is $\text{Log } \Delta$ where Δ is the average gas density in each column in units of the critical gas density. The red circles represent accreting black holes. The size of each symbol is proportional to the logarithm of the flux. The circle in the bottom left corner represents the magnitude of the background flux coming in from outside the cut out region. The radiation field is dominated by the central black hole and the background flux.

Table 1. Summary of the Sources of Ionizing Radiation

Number & Type	$\Sigma \dot{N}_{\gamma} [1.0 \times 10^{50} \text{ s}^{-1}]$	α
1 Central BH	4.84×10^6	1.76
Background	1.27×10^6	1.00
81 Minor BHs	9.72×10^4	1.76
429 Stellar	2.12×10^3	1.00

lite accreting black holes, and the star forming galaxies. We have summarized the fiducial luminosities in Table 1. Note that 98.4% of the ionizing photon flux comes from the background and the central black hole. There is a 1.60% contribution from the minor black holes and a 0.03% contribution from the young stellar clusters. For this reason, we have chosen to include only the background and the central source in our models. Below we describe how we calculate the photon flux from these sources.

We assume that, above the HI ionizing threshold, the spectra of all our source populations can be modeled with power laws of the form,

$$J = J_{\text{HI}} \left(\frac{\nu}{\nu_{\text{HI}}} \right)^{-\alpha}, \quad (1)$$

where J is a specific intensity with units of $\text{ergs cm}^{-2} \text{ s}^{-1} \text{ Hz}^{-1} \text{ sr}^{-1}$.

4.1 Accreting Black Holes

The GADGET simulation tracks the formation and accretion history of black holes. The bolometric luminosity of each black hole is related to its accretion rate through an efficiency parameter $\eta = L_b / \dot{M}_{\text{BH}} c^2$. We take as our fiducial value $\eta = 0.1$ which is the mean value for radiatively efficient accretion onto a Schwarzschild black hole (Shakura & Syun'yaev 1973). In §7 we also consider models with smaller and larger radiative efficiencies. In the GADGET simulation a small fraction of this energy is thermally coupled to the nearby gas $\dot{E}_{\text{feed}} = \epsilon_f L_b$. A value of $\epsilon_f = 0.05$ brings the simulation into agreement with observations of the $M_{\text{BH}} - \sigma$ relationship (Di Matteo et al. 2005).

This population of sources consists of a dominant central black hole and tens of black holes with smaller accretion rates surrounding it (see Figures 2 and 3). For each of these black holes we calculate a B band luminosity using the bolometric corrections of Marconi et al. (2004). To translate this to a luminosity at the Hydrogen ionizing threshold we use a broken power law spectrum with spectral index $\alpha_{\text{OP}} = 0.44$ in the optical part of the spectrum and $\alpha_{\text{UV}} = 1.76$ in the UV part with the break at 1200 Angstroms. Given the luminosity at the ionizing threshold, we integrate the power law from 1 to 36 Rydbergs to calculate the number of ionizing photons per second. The choice of cutoff frequency is dictated by a deviation from the UV power law above ≈ 36 Rydbergs in the quasar template spectra and the fact that high energy X-ray photons above 36 Rydbergs have mean free paths much longer than our box size.

With a box of this size, it is not possible to examine the full quasar luminosity function due to the lack of rare objects however, DeGraf et al. (2009) examine its faint end using the base hydrodynamic simulation discussed above and two similar simulations.

4.2 UV Background

The ionizing background is a combination of the ionizing radiation produced by quasars and star forming galaxies that reside outside our simulation volume. Estimating the magnitude of this radiation field observationally is challenging. In general, there have been two approaches. One involves integrating observed luminosity functions and another involves inferring the background from the HI photoionization rate calculated using quasar absorption lines. The latter method has the advantage that the absorption lines probe the local $z = 3$ gas.

The fundamental observable we've used to calibrate the background flux used in our simulation is the Lyman α forest measurements of Faucher-Giguère et al. (2008) (FG08) who calculate a mean Hydrogen photoionization rate $\Gamma_{\text{HI}} = (0.59 \pm 0.07) \times 10^{-12} \text{ s}^{-1}$ at $z=3$. The Hydrogen photoionization rate for a uniform background with spectral index α is given by,

$$\Gamma_{\text{HI}} = 4\pi \int_{\nu_{\text{HI}}}^{\infty} \frac{d\nu}{h\nu} \sigma_{\text{HI}} \left(\frac{\nu}{\nu_{\text{HI}}} \right)^{-3} J_{\text{HI}} \left(\frac{\nu}{\nu_{\text{HI}}} \right)^{-\alpha} \quad (2)$$

where h is Planck's constant, σ_{HI} is the photoionization cross section of Hydrogen at the Lyman limit, and J_{HI} is the angle averaged specific intensity. Integrating and solving for J_{HI} we get,

$$J_{\text{HI}} = \frac{\Gamma_{\text{HI}} h (\alpha + 3)}{4\pi \sigma_{\text{HI}}} \quad (3)$$

Using the slope we adopt for our background spectrum $\alpha = 1.00$ gives a numerical value of $J_{\text{HI}} = 2.35 \times 10^{-22} \text{ ergs Hz}^{-1} \text{ s}^{-1} \text{ cm}^{-2}$ and implies a photon number density,

$$n_{\gamma} = \frac{4\pi}{c} \int_{\nu_{\text{HI}}}^{\infty} \frac{J_{\text{HI}} \left(\frac{\nu}{\nu_{\text{HI}}} \right)^{-\alpha}}{h\nu} d\nu \quad (4)$$

For a uniform UV background n_{γ} along with the spectral index α completely characterizes the radiation field.

The emissivity ϵ , of the sources is connected to the background intensity J_{HI} through the mean free path l_{HI} of the photons. In the Local Source approximation, sources separated from a given point by more than one mean free path have their contribution highly attenuated (see Schirber & Bullock 2003). In this regime the emissivity is expressed simply as,

$$\epsilon = 4\pi \frac{J_{\text{HI}}}{l_{\text{HI}}}. \quad (5)$$

This mean free path is calculated in Faucher-Giguère et al. (2008) as

$$l_{\text{HI}} = 85 \left(\frac{1+z}{4} \right)^{-4} \text{ proper Mpc} \quad (6)$$

At $z = 3$, approximately half of the ionizing photons in the background originate in star forming regions. This emissivity and the relatively small volume of our simulation compared to l_{HI} imply that less than 1 in 1000 ionizing photons we consider originate in star forming regions within the simulation.

5 IONIZING RADIATION MODELS

The ionization state of Hydrogen is a balance between photo/collisional ionizations and recombinations. In particular, the Hydrogen ionization fraction $x = n_{\text{HI}}/n_{\text{H}}$, evolves according to the equation

$$\frac{dx}{dt} = [\Gamma_{\text{HI}} + \gamma(T) n_{\text{e}}(x)]x - \alpha(T) n_{\text{e}}(x) x, \quad (7)$$

where Γ_{HI} is the photoionization rate, γ is the collisional ionization rate, α is the recombination rate, and n_{e} is the electron number density. If we decompose n_{e} into a part due to Hydrogen ionizations and a part due to Helium and metal ionizations $n_{\text{e}} = (x + y)n_{\text{H}}$ we can rewrite the above equation as,

$$\begin{aligned} \frac{dx}{dt} &= Rx^2 + Qx + P, \\ R(t) &= (\gamma + \alpha)n_{\text{H}} \\ Q(t) &= \Gamma_{\text{HI}} - \gamma n_{\text{H}} + (\gamma + \alpha)n_{\text{HY}} \\ P(t) &= -(\Gamma_{\text{HI}} + \gamma n_{\text{HY}}) \end{aligned} \quad (8)$$

This is a Riccati equation and the equilibrium solution is given by the positive root of the quadratic formula. In a pure Hydrogen and Helium gas, the variable y is bound between $y = 0$ for completely neutral Helium and $y = (1 - X)/2X$ for fully ionized Helium, where X is the Hydrogen mass fraction of the gas.

5.1 Semi Analytic Model

For comparison with our ray tracing results, we calculate the neutral Hydrogen field using several simplifying assumptions. Given a density field n_{H} , a temperature field T , an electron abundance from Helium and metals y , and a photoionization rate Γ_{HI} , we can analytically calculate the equilibrium Hydrogen ionization fractions using equation (8). We take the first three quantities from the base hydrodynamic run and supply the photoionization rate by hand.

The simplest model contains only the unshielded background UV field. This amounts to setting $\Gamma_{\text{HI}} = \Gamma_{\text{HI}}^{\text{Bgn}} = 0.59 \times 10^{-12} \text{ s}^{-1}$ for each particle. To include the central source we add to this background an inverse squared contribution from the quasar.

$$\begin{aligned} \Gamma_{\text{HI}}^{\text{QSO}} &= \frac{1}{4\pi r^2} \int_{\nu_{\text{HI}}}^{\infty} \frac{d\nu}{h\nu} \sigma_{\text{HI}} \left(\frac{\nu}{\nu_{\text{HI}}} \right)^{-3} L_{\text{HI}} \left(\frac{\nu}{\nu_{\text{HI}}} \right)^{-\alpha_{\text{UV}}} \\ &= \frac{L_{\text{HI}} \sigma_{\text{HI}}}{4\pi r^2 h (\alpha_{\text{UV}} + 3)} \end{aligned} \quad (9)$$

where L_{HI} is the luminosity density of the quasar at one Rydberg in units of $\text{ergs s}^{-1} \text{ Hz}^{-1}$ and α_{UV} is the spectral slope in the UV part of the quasar spectrum. For these models the photoionization rate $\Gamma_{\text{HI}} = \Gamma_{\text{HI}}^{\text{Bgn}} + \Gamma_{\text{HI}}^{\text{QSO}}(r)$. Finally, we include a set of models in which $\Gamma_{\text{HI}} = \Gamma_{\text{HI}}^{\text{Bgn}} + \Gamma_{\text{HI}}^{\text{QSO}}(r)$ for particles below a given gas density threshold and zero above it. These models are labeled by the density threshold in units of the critical gas density on a logarithmic scale (e.g. " $\Delta = 4.0$ " has gas with density greater than ten thousand times the mean shielded).

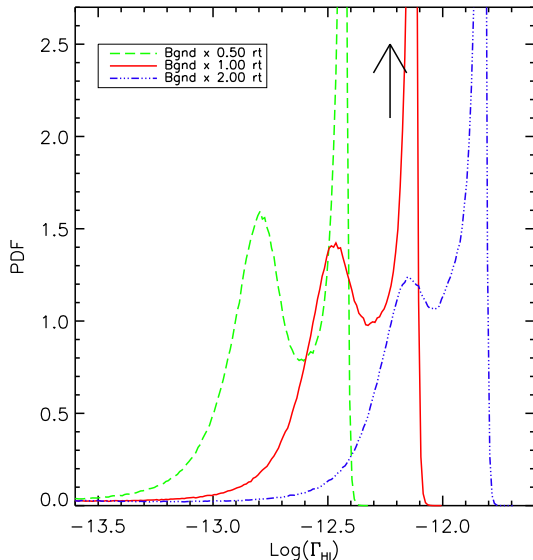


Figure 4. Mass weighted probability distribution of Γ_{HI} for several background only ray tracing models. The arrow indicates the observed value at $z = 3$ from FG08. The width of the arrow head indicates the $1\text{-}\sigma$ error bars on their measurement. For a completely uniform background this distribution would be a delta function at the arrows position. The primary peaks are due to the mildly over dense IGM while the smaller secondary peaks and tails towards small Γ_{HI} are due to self shielding.

5.2 Ray Tracing Models

For these models we calculate the transfer of ionizing radiation emitted from the central quasar inside our computational volume as well as a background flux sent in through the boundaries. These models naturally account for the self shielding of dense particles. The flux that constitutes the background is calibrated by running several ray tracing models without the central quasar contribution. The flux that most nearly reproduces the Γ_{HI} observed by FG08 is set as the fiducial background strength (see Figure 4). This flux is used in all the models that include the contribution from the central quasar. The luminosity of the black hole is determined by the accretion rate from the base hydrodynamic simulation. We have introduced an arbitrary scaling factor into the central quasar luminosity to model the effect of changing the efficiency with which accreted matter is converted into ionizing photons. These models are labeled “GADGET + SPHRAY”.

6 RESULTS

In this section we discuss the radiative transfer results and make our comparisons between the ray tracing and semi analytic models.

6.1 Neutral Fractions

First we will take the global view and examine the distribution of neutral fractions for all the particles in our simulation volume. In Figure 5, we show this distribution for sev-

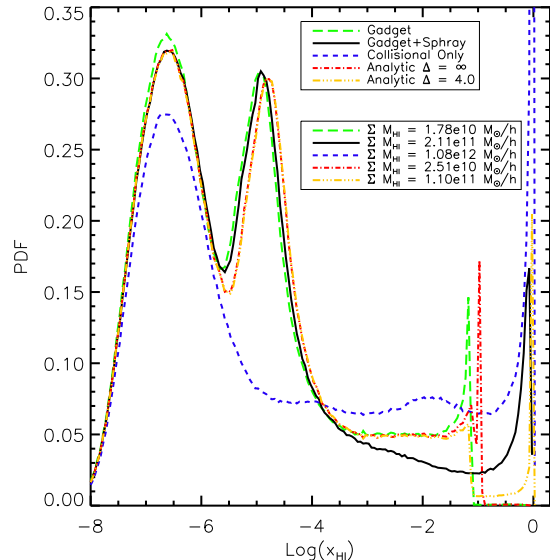


Figure 5. Mass weighted probability distribution of x_{HI} for several background only models. The dashed green line indicates the distribution taken directly from the GADGET simulation. The solid black line indicates the distribution after the GADGET data has been post processed with SPHRAY using the fiducial background strength. The dashed blue line is a semi analytic model in which the photoionization rates were set to zero everywhere and only collisional ionizations were considered. The red dash-dot line is a semi analytic model with the shielding density threshold set to infinity (i.e. zero shielding) while the orange dash-dot-dot line is identical except that the shielding threshold has been set to ten thousand times the mean density. The total amount of neutral Hydrogen in each model is indicated in the legend.

eral models that include only a UV background. The triple peaked structure of this distribution is common to all models, the left peak being due mostly to collisional ionizations, the central peak due to photoionizations in the IGM and the right peak formed by particles self shielding from the ionizing radiation. The vast majority of the neutral material resides in the self shielding peak and we have indicated in the Figure the total amount of neutral Hydrogen for each model. We present these background only results to demonstrate the consistency between the original GADGET simulation, the radiative transfer post processing results, and the semi analytic models away from the self shielding region. This is the reason why a detailed treatment of self shielding is not necessary for studies of the Lyman- α forest, but is necessary for studies of denser systems.

In Figure 6, we show the x_{HI} distribution for several radiation models that include not only a UV background but the central quasar as well. The results directly from the GADGET simulation and those that include only collisional ionizations are reproduced from Figure 5 for reference. The semi analytic model in which particles with a total gas density above $\text{Log } \Delta = 4.0$ are completely shielded reproduces the total amount of neutral Hydrogen present in the fiducial ray tracing model, however the self shielding peak is artificially concentrated at very high neutral fractions. We will see how this difference affects the radial HI profiles in the

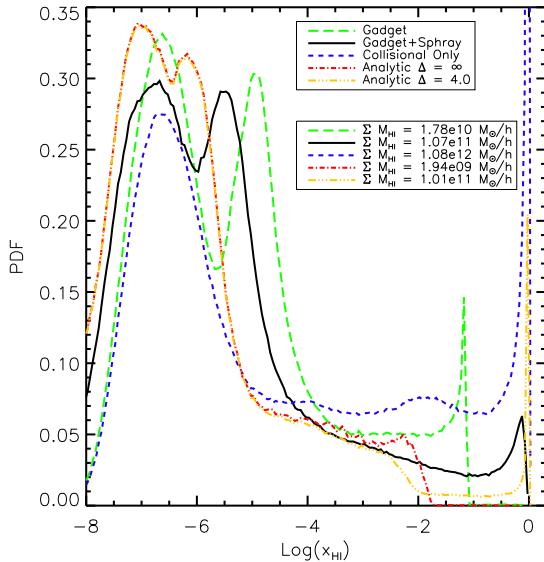


Figure 6. Mass weighted probability distribution of x_{HI} for several background plus quasar models. The solid black line indicates the distribution after the GADGET data has been post processed with SPHRAy using the fiducial background and quasar luminosities. The red dash-dot line is a semi analytic model with the shielding density threshold set to infinity (i.e. zero shielding) while the orange dash-dot-dot-dot line is identical except that the shielding threshold has been set to ten thousand times the mean density. The dashed green line indicates the distribution taken directly from the GADGET simulation which included only a uniform UV background. The dashed blue line is a semi analytic model in which photoionization rates were set to zero and only collisional ionizations were considered. These last two models do not include a central quasar component (or any photoionizations in the latter case) and are shown only for reference. The total amount of neutral Hydrogen in each model is indicated in the legend.

next section, the Δ vs. x_{HI} distribution in § 6.3 and the HI column densities in § 6.4. The completely unshielded semi analytic model produces no particles with neutral fractions above $x_{\text{HI}} \approx 0.02$ and contains only 2 % of the neutral Hydrogen present in the fiducial ray tracing model.

6.2 Radial Distributions

Here we show how the neutral fraction PDFs translate into radial neutral mass distributions. In Figure 7, we plot the cumulative HI mass within a given radius for the same models as in Figure 6. As was mentioned in the previous section, the semi analytic model in which particles with a gas density $\text{Log } \Delta > 4.0$ are shielded yields the same total neutral mass as the fiducial ray tracing model, but the radial profiles are significantly different. This means that self shielding effects are important not only for absorption line measurements but also for HI emission observations attempting to connect the HI mass with the underlying total density field.

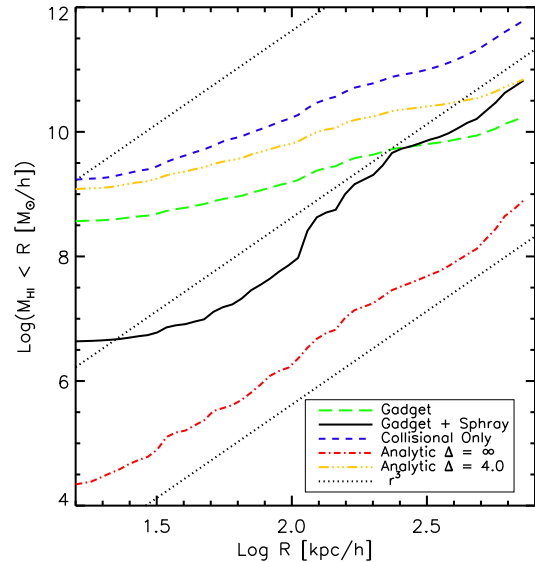


Figure 7. Cumulative HI distribution. Shown is the neutral Hydrogen mass [M_{\odot}/h] within a given radius R [proper kpc/h] for several background plus quasar models. The solid black line indicates the distribution after the GADGET data has been post processed with SPHRAy using the fiducial background and quasar luminosities. The red dash-dot line is a semi analytic model with the shielding density threshold set to infinity (i.e. zero shielding) while the orange dash-dot-dot-dot line is identical except that the shielding threshold has been set to ten thousand times the mean density. The dashed green line indicates the distribution taken directly from the GADGET simulation which included only a uniform UV background. The dashed blue line is a semi analytic model in which photoionization rates were set to zero and only collisional ionizations were considered. These last two models do not include a central quasar component (or any photoionizations in the latter case) and are shown only for reference. We have also added several lines that go as r^3 for reference.

6.3 Density vs Neutral Fraction

Here we examine the relation between neutral fraction and total gas density. We show this distribution for three semi analytic models and our ray tracing model in Figure 8. Naively, one might associate the densest gas with the most neutral gas, however this is not the case due to the high temperatures produced by shock heating and feedback which cause collisional ionizations. Instead, most of the neutral material is in a peak at approximately 10,000 times the mean density where shielding can occur and temperatures remain in the tens of thousands of degrees.

In the third panel we show the results for a semi analytic model with a shielding threshold at $\text{Log } \Delta = 2.8$. We include this panel not because this is a realistic density threshold, but rather to show how the distribution above the threshold compares to the ray tracing results in the last panel.

6.4 Neutral Hydrogen Column Densities

We have calculated the distribution of neutral Hydrogen column densities through the 1500 kpc/h (physical) simulation volume. To do this, we collapsed all the gas along the z -axis and then calculated the column density on each of $2048 \times$

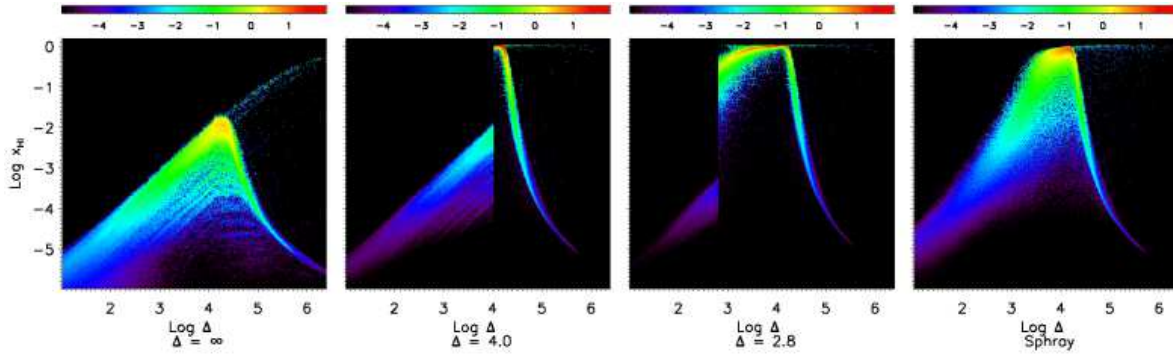


Figure 8. Density vs Neutral Fraction distribution for several radiative models. All of them include the fiducial strength background and central quasar. The panel on the left is a semi analytic model with no shielding, the next two are semi analytic models with shielding thresholds at $\Delta = 4.0$ and 2.8 . The last panel is the fiducial ray tracing model. Shown is the neutral mass probability density distribution in $\text{Log } \Delta - x_{\text{HI}}$ space where Δ is the gas density in units of the baryon critical density and x_{HI} is the neutral fraction [i.e. an integral over the plane shown will give unity]. The color bar is logarithmic such that a unit difference between two pixels indicates a factor of ten difference in neutral mass.

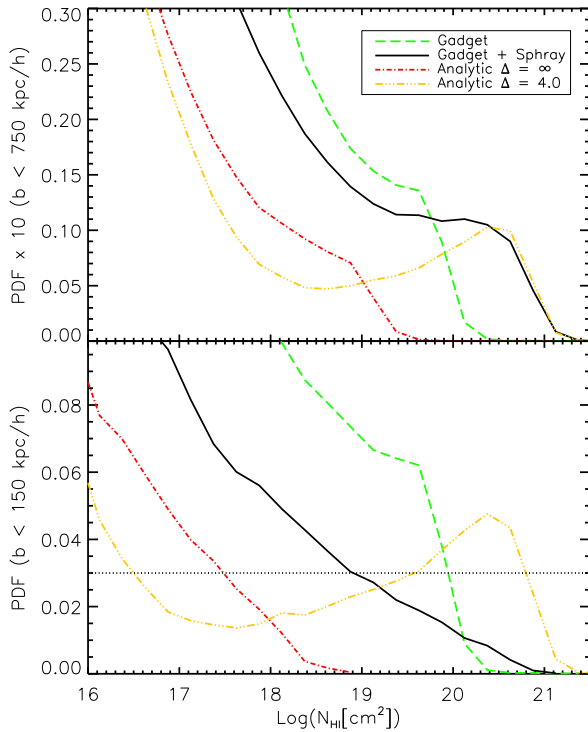


Figure 9. Distribution of Neutral Hydrogen Column densities obtained by collapsing the 1500 kpc/h simulation volume along the z axis. The top panel includes all lines of sight with an impact parameter $b < 750$ kpc/h, while the bottom panel is restricted to those lines of sight with an impact parameter $b < 150$ kpc/h. The GADGET model does not include the UV field from the central quasar. We have indicated the maximum y -value in the upper panel with a horizontal line in the lower panel.

2048 pixels on this collapsed plane interpolating from the SPH smoothing kernels. This leads to 0.732 pc/h between hypothetical lines of sight.

In Figure 9 we show the probability distribution function of column densities for all the lines of sight with impact parameters $b < 750$ kpc/h (top panel) and $b < 150$ kpc/h

(bottom panel). The peak of this distribution is off the plot to the left as most of the area on the collapsed plane is in the IGM, however in this work we are concerned with the optically thick systems above $\text{Log } N_{\text{HI}} = 17.2$.

We examine this distribution in four models. Three of these include the central quasar and background UV fields and one, the direct GADGET output, only includes a background UV field. This lack of a central source in the latter model causes the PDFs in the top and bottom panels to have the same shape as the restriction to small impact parameters does not select a region of space with an enhanced UV field. It is interesting to note that the $\Delta = 4.0$ semi analytic model shows this same radial independence. Examining Figures 7 and 14, it is clear that the semi analytic model with zero shielding and the ray tracing GADGET + SPHRAY model have cleared almost all the HI from the central 100 kpc/h. In the $\Delta = 4.0$ model, this HI is largely filled back in which removes the radial dependence. This highlights the main problem of using a strict density threshold criteria for semi analytic self shielding in the presence of point sources. In this case it is clear that this choice of threshold produces too much shielding close to the source and too little shielding at larger radii.

In the top panel of Figure 9, each model demonstrates, albeit to varying degrees, a power law at low column densities followed by a flattening and then a cut off at higher column densities. This behavior was examined by Zheng & Miralda-Escudé (2002) (see Figure 2 in that work for their N_{HI} distributions) using a model in which a spherical and isothermal gaseous halo is illuminated by a cosmic background UV field and ascribed the flattening feature to self shielding. Our ray tracing model, with the most realistic treatment of self shielding, produces the largest flat section, however the semi analytic $\Delta = \infty$ model and the direct GADGET output also contain slight flattening features while neither model includes any self shielding. In addition, this flattening feature is washed out near the quasar for the semi analytic $\Delta = \infty$ and the ray tracing model (bottom panel). This means the intrinsic density field is such that it produces a slight flattening feature and in the presence of mild UV fields this feature is enhanced by self shielding. How-

ever, once the UV field becomes too strong, the feature is completely washed away.

A simple statistic to derive from these data is the covering fraction of pixels above a given column density threshold $f_c^{N_{\text{HI}}}$ defined as the number of pixels above N_{HI} divided by the total number of pixels. In Table 2, we report these covering fractions f_c for lines of sight with $\text{Log } N_{\text{HI}}$ above 17.2 and 19.0 for the same impact parameter cut offs as above. We also include the covering fractions reported in Hennawi et al. (2006). We allow for various central quasar luminosities in our ray tracing models and several shielding thresholds in our semi analytic models. These numbers do not take into account the fact that the observational sample of HP06 does not uniformly cover impact parameter space, but we address this issue in §7. One can see from the table that shielded semi analytic models that manage to reproduce the covering fraction from the ray tracing models do not reproduce the total HI mass in the cylinder. One can also see that both of our models fall short of the covering fractions implied by HP06. There are several explanations for this and they will be discussed fully in §7.

6.5 Photoionization Rate

We examine the radial and angular dependence of the photoionization rate from our fiducial GADGET + SPHRAIN model in Figures 10 and 11. The PDFs in Figure 10 serve to illustrate two things. The equal spacing between peaks demonstrates the general inverse square character of Γ_{HI} and the width of the distributions on each shell show the effects of partial shielding from the ray tracing run. This is far from a binary “on” or “off” distribution. We note that several authors have utilized more detailed semi analytic prescriptions than ours for self shielding, however without a detailed radiative transfer model to compare with, the success of these models at reproducing the true shielding is in question. We have indicated the photoionization rate which an unshielded particle would feel at each radii using vertical lines.

To visualize the angular dependence of Γ_{HI} on these shells in the fiducial ray tracing run, we use the HealPix algorithm to create Mollweide projections of this quantity at the same radii as in Figure 10. The self shielded particles show up as dark spots and some shadowing is revealed as a persistent dark spot in the lower left of each diagram.

A radiation field that is restricted to limited solid angles would help explain the non-detection of the transverse proximity effect (e.g. Croft 2004). Because large dark matter halos which host quasars typically lie at the intersection of several filaments, one might expect that isotropic emission could be reduced in some solid angles by filtering through the surrounding density field. We have shown here that this is not the case and that if the radiation from quasars is restricted to certain solid angles that obscuration by optically thick material near the black hole (below the resolution of our simulation) is a more likely explanation.

7 COMPARISON TO OBSERVATIONS

In the first of a series of papers entitled “Quasars Probing Quasars” Hennawi et al. (2006) have compiled a catalogue

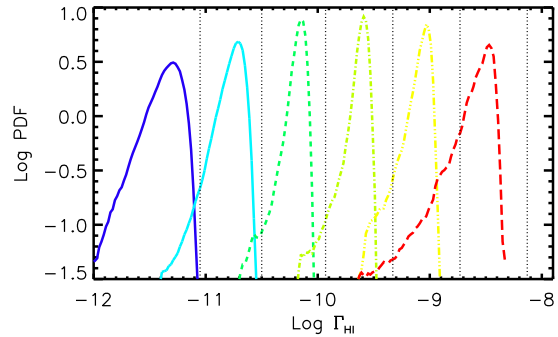


Figure 10. Probability distribution function of Γ_{HI} on a series of spherical shells. The radii are $R = 12.5, 25, 50, 100, 200,$ and 400 kpc/h from the central black hole. The equal spacing of the peaks indicates a general r^{-2} behavior and the width indicates shadowing and shielding. We have indicated the photoionization rate which an unshielded particle would feel at each radii using vertical lines.

of quasars with small angular separations on the sky. This sample can be used to study the environment of the foreground quasars using the absorption lines in the spectra of the background quasars. Specifically, they measure the number of sight lines that intersect absorbers with column densities above $\text{Log } N_{\text{HI}} = 17.2$ and $\text{Log } N_{\text{HI}} = 19$ corresponding to Lyman Limit systems and Super Lyman Limit Systems.

We now make a comparison of our radiative transfer modeling with these observations. This is necessarily a crude comparison because we are limited to a single quasar (albeit simulated at several luminosities) situated in a dark matter halo which is most likely less massive than those hosting the quasars in the HP06 sample. In Figure 12, we show the distribution in luminosities for the $N_{\text{los}} = 61$ foreground quasars in their sample whose sight lines have impact parameters that would place them inside our cut out proximity zone.

Hennawi et al. (2006) report the maximum enhancement of the UV background due to the foreground quasars in their sample as,

$$g_{UV} = 1 + \frac{F_{QSO}}{F_{UV}} \quad (10)$$

where F_{QSO} is the number flux of ionizing photons at the position along the line of sight closest to the foreground quasar and F_{UV} is the number flux of photons at the same position due to the UV background. To translate this into an upper limit for the number of ionizing photons emitted by the foreground quasar per second we use,

$$N_{QSO} = 4\pi b^2 F_{QSO} = 4\pi b^2 F_{UV}(g_{UV} - 1) \quad (11)$$

where b is the impact parameter of the line of sight to the background quasar. We have used a spectral slope of $\alpha = 1.8$ and a luminosity density at the Hydrogen ionizing threshold of $J_{\text{HI}} = 5.0 \times 10^{-22}$ from Haardt & Madau (1996) to calculate F_{UV} .

Also shown in Figure 12 is the mean value of the HP06 sample luminosities (black horizontal solid line) and the seven quasar luminosities we used in our simulations (blue horizontal dashed lines). The vertical cyan lines in the plot

Table 2. Neutral Hydrogen Statistics.

Radiative Model	Quasar Luminosity	Shielding Threshold (Δ)	$b < 750$ kpc/h			$b < 150$ kpc/h		
			$\text{Log } \Sigma M_{\text{HI}} [M_{\odot}/h]$	$f_c^{17.2}$	f_c^{19}	$\text{Log } \Sigma M_{\text{HI}} [M_{\odot}/h]$	$f_c^{17.2}$	f_c^{19}
HP06	$< N_{qso} > = 0.5$	NA	NA	24.6	16.4	NA	75.0	50.0
Ray	0.03125	NA	11.12	9.24	3.25	10.26	25.7	10.6
	0.06250	NA	11.10	8.95	3.12	10.17	23.3	9.11
	0.01250	NA	11.07	8.50	2.94	10.05	20.2	7.37
	0.02500	NA	11.02	7.90	2.70	9.872	17.1	5.67
	0.50000	NA	10.96	7.15	2.40	9.619	13.9	4.03
	1.00000	NA	10.86	6.38	2.06	9.284	11.7	2.70
r^{-2}	1.00000	3.4	11.28	5.07	3.43	10.55	21.2	14.8
	1.00000	3.7	11.14	3.64	2.36	10.41	15.1	10.7
	1.00000	4.0	10.86	2.85	1.53	10.13	10.1	7.04
	1.00000	4.3	9.805	2.38	0.510	9.079	5.39	1.97
	1.00000	7.0	9.124	2.23	0.126	7.225	2.56	0.00

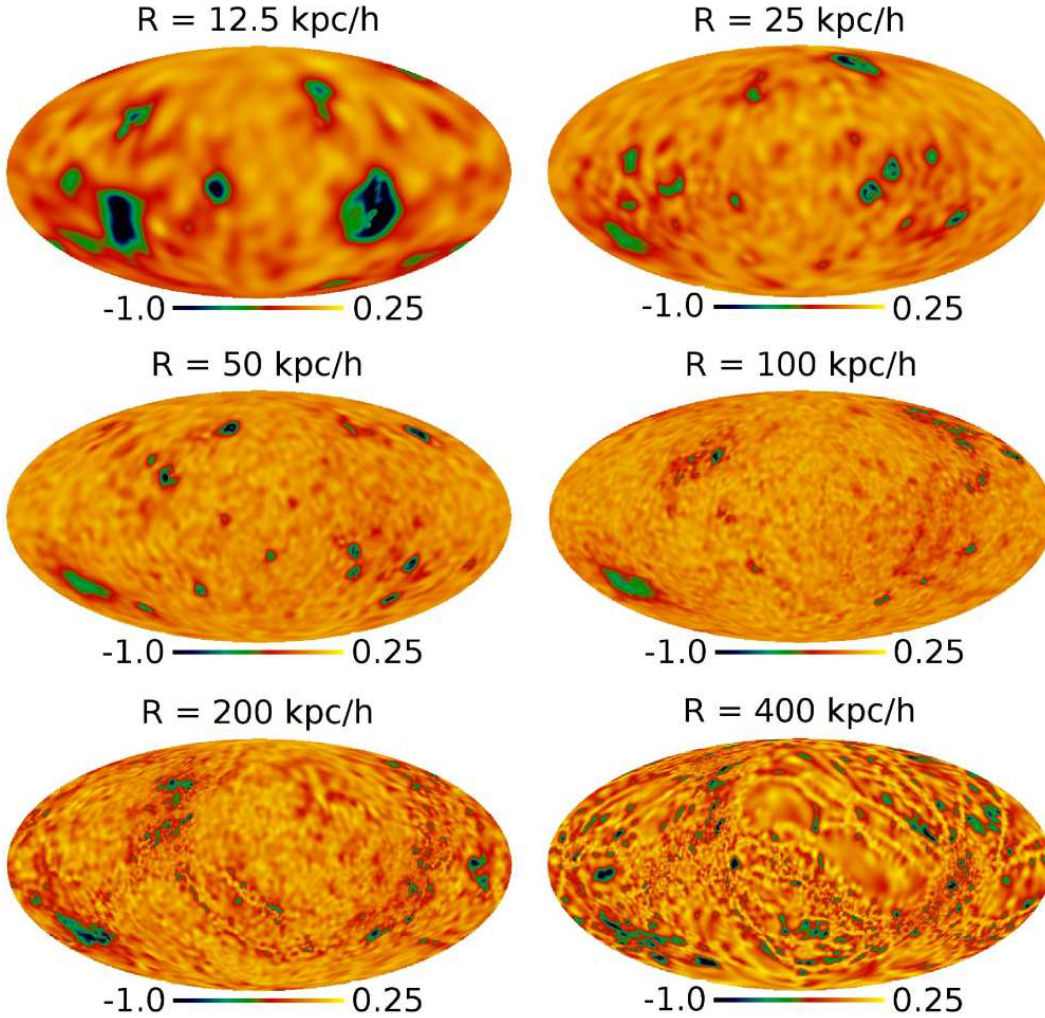


Figure 11. Mollweide projections showing the fluctuation of $\text{Log } \Gamma_{\text{HI}}$ on spherical shells at several radii. From left to right and top to bottom, the radii are $R = 12.5, 25, 50, 100, 200,$ and 400 kpc/h from the central black hole. These are the same radii that are shown in Figure 10 and the fluctuations are around the peak at each radius in that plot. A persistent shadow can be seen in the lower left region of each plot.

indicate the impact parameter bins we used to construct a sample of $N_{\text{mock}} = 1000$ sets of $N_{\text{los}} = 61$ lines of sight with the same distribution in impact parameter as their sample.

In Figure 13, we present our comparison. For the fiducial ray tracing model, we count the number of lines of sight above threshold in each of the N_{mock} groups and histogram the values. We repeat this procedure for each of the seven simulated quasar luminosities (see Figure 12) and plot the results as thin yellow lines in the upper left ($\text{Log } N_{\text{HI}}^{\text{th}} = 17.2$) and lower left ($\text{Log } N_{\text{HI}}^{\text{th}} = 19.0$) panels. Overlaid on these lines in thick black is the luminosity weighted average of each bin. The weighting is done by determining the fraction of HP06 quasars that is nearest to each simulated quasar luminosity. In the second and third columns we repeat this procedure for two semi analytic models. The last two columns show the same thing for ray tracing runs that include only a UV background sent in from outside the box (fiducial in fourth column and half the fiducial in fifth column). These two background intensities produce photoionization rates within $\approx 3\sigma$ of the value determined by FG08 (see Figure 4). We will use these panels to discuss the effects of obscuration and periodic emission shortly. We have indicated the observed values from HP06 with vertical dashed lines and the peak of the luminosity weighted average from the first panel (GADGET + SPHRAY ray tracing runs) with arrows in each panel. In all cases which include contributions from the central quasar, we fall short of the observed incidence of optically thick absorbers. There are several plausible explanations for this.

Before we present these explanations we briefly discuss the pixel maps used to generate Figure 13. First, we note that the semi analytic model that comes closest to reproducing the observational results is unrealistic in terms of the distribution of HI. In Figure 14 we show the projected column densities and the positions of galaxies identified in the base hydrodynamic simulation. The top row is the direct GADGET output, the top middle row is the fiducial ray tracing GADGET + SPHRAY run, the bottom middle row is a semi analytic model with no shielding and the bottom row is the $\text{Log } \Delta = 4.0$ semi analytic run. The columns show magnifications of the central region.

7.1 Proximate Density Field - Host Halo

The most straightforward explanation for the disagreement we see is that our single density field is not representative of the proximity zones in the HP06 sample. The neutral Hydrogen density field is determined by a combination of the total baryonic overdensity in the proximity zone, the background radiation field, and the ionizing flux from the central point source. We have taken account of the various quasar luminosities by running multiple models, however we are restricted, in this study, to a single density field.

The mass of the dark matter halo hosting our central quasar is $M_{\text{Halo}} = 5.25 \times 10^{12} h^{-1} M_{\odot}$. Observations of the clustering of quasars (e.g. Porciani et al. 2004; Croom et al. 2005; Shen et al. 2007; Coil et al. 2007; Shen et al. 2009) imply a minimum quasar host halo mass between 10^{12} and $10^{13} h^{-1} M_{\odot}$ with a typical mass closer to $10^{13} h^{-1} M_{\odot}$. In the third of the Quasars Probing Quasars series of papers, Prochaska & Hennawi (2009) examine a single representative quasar pair in detail. In this analysis, they use a mass

of $M_{\text{Halo}} = 2.01 \times 10^{13} h^{-1} M_{\odot}$ for the foreground quasar's host halo mass. Therefore, it is plausible that our dark matter host halo is a factor of four less massive than the typical host halo from the HP06 sample.

Kim & Croft (2008) have constrained host halo masses at a mean redshift of $z = 3$ using the mean transmitted flux in the Ly- α forest and find agreement with the previous works mentioned above. In addition, they have shown that the baryonic over density within a given radius is an increasing function of halo mass. Specifically, in Figure 2, they show an increase in baryonic overdensity by a factor of 3.66 as dark matter halos range from 1.6×10^{11} to $5.1 \times 10^{12} M_{\odot} h^{-1}$ using a $100 h^{-1} \text{Mpc}$ cosmological simulation. Our fiducial ray tracing run peaks at a value of 5 absorbers (top left panel in Figure 13) with column densities $\text{Log } N_{\text{HI}} \geq 17.2$. HP06 observe 15 lines of sight with impact parameters that would put them in our cut out region above this threshold. Using a simple linear scaling from the data of Kim & Croft (2008) in the relevant mass range and for the number of absorbers with overdensity, we estimate the representative dark matter host halo mass in the HP06 sample as $M = 1.92 \times 10^{13} M_{\odot} h^{-1}$. This agrees well with the value used in Prochaska & Hennawi (2009).

7.2 Unresolved Clumping

Aside from the fact that our theoretical sample is limited to a single density field, the dynamic range required to resolve small scale clumping of gas in a cosmological volume is extreme. In the base hydrodynamic simulation, the distribution of smoothing lengths peaks at $\approx 8.5 h^{-1} \text{kpc}$ over the whole simulation, and $\approx 850 h^{-1} \text{pc}$ or 10^{-4} of the full box size in dense regions. In a follow up paper to HP06, Prochaska & Hennawi (2009) estimate the size of a single absorber as 10-100 pc while the smallest smoothing length in our cutout proximity zone is $150 h^{-1} \text{pc}$. Better resolving this small scale clumping would increase the incidence of optically thick absorbers and increase the column density of those already identified. While it would be a very large undertaking to simulate an entire cosmological volume at the necessary resolution, it is feasible to re-simulate a handful of proximity zones at higher resolutions. On the other hand, we could enlarge our cut out region further and use semi-analytic treatments of this clumping by requiring our global (as opposed to that around a single quasar) distribution of Damped Lyman- α systems to match observations. In practice, simulations like these are used together to calibrate one another and both are something we plan to do in the future.

7.3 Obscuration and Duty Cycle

In unified theoretical models of AGN and quasars (e.g. Antonucci 1993), the emission from the accretion disc and broad line regions is obscured over a certain solid angle by an optically thick torus. The inhomogeneities this could induce in the Lyman α forest have been theoretically investigated by Croft (2004). In addition, Hennawi & Prochaska (2007) find evidence of this obscuration by comparing the incidence of optically thick absorbers in foreground quasar lines of sight with the transverse lines of sight to background quasars. Our simulated sources emit isotropically and so,

even with self shielding, there could be large solid angles in which we are overestimating the photoionization rate. To get an idea of the magnitude of this effect we present the background only panels in Figure 13 (columns 4 and 5). These backgrounds bracket the value calculated in FG08 and are both within 3σ of the backgrounds present at the bulk of the redshifts in the HP06 sample. If the radiation is only present within certain solid angles, the incidence of absorbers in our single density field will lie somewhere between the ray tracing panel and one of the background only panels. This could account for a non negligible part of the discrepancy we see as 1.8% and 5.3% (columns 4 and 5) of the mock groups of sight lines overlap the HP06 data.

In a similar way, a central black hole undergoing an episode of accretion that lasts less than the light crossing time of the region considered can lead to large volumes where we have overestimated the photoionization rate. The light crossing time for our cutout region, from the center of the cube to the corner, is $t_X \approx 6$ Myr. The lower limit on episodic emission from quasars is set by observations of the line of sight proximity effect in the Ly- α forest (e.g. Bajtlik et al. 1988; Scott et al. 2000) and is equal to the photoionization equilibration time of the IGM, $t_{eq} = 10^4$ years (Martini & Weinberg 2001). If the central source were on for a time t_{on} where $0.01 \leq t_{on} \leq 6$ Myr then certain radii would not have felt the enhanced UV field from the central source yet.

7.4 Velocity Offsets

It is straightforward to determine the angular separation of two objects on the sky. Due to redshift distortions, it is much more difficult to determine their separation in the radial direction. This problem is exacerbated for gas near large overdensities where it has large infall / outflow velocities. The definition of proximate DLA in the HP06 sample is systems with absorber redshifts within 3000 km/s of the emission redshift of the foreground quasar. Due to this uncertain radial separation, we have included all absorbers in the observational sample that satisfy the impact parameter requirements of our cut out region. This includes some absorbers from the HP06 sample in our comparison that would not actually be in our cutout region. A larger cut out region would allow us to better model these errors.

8 CONCLUSION AND DISCUSSION

In this paper, we have presented a detailed model for the neutral hydrogen gas in the proximity zone of a quasar powered by accretion onto a super massive black hole. To do this, we combined a cosmological hydrodynamic GADGET simulation of the formation and growth of black holes with a detailed radiative transfer post processing code SPHRAY. We focused our attention on self shielding of the neutral gas and, by construction, the contribution from a local central source. Much of the previous work on Lyman Limit and Damped Lyman α systems ignored the contribution from point sources assuming that the background field dominates. This is true, on average, for absorbers less dense than Lyman Limit systems but is not true for the more dense absorbers

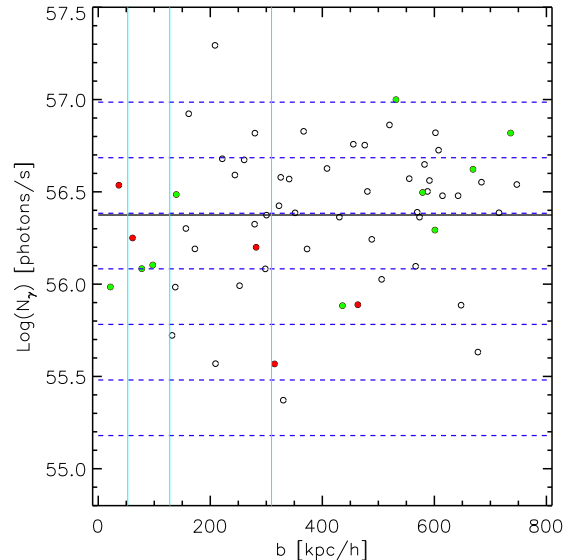


Figure 12. Maximum foreground quasar luminosity vs impact parameter for the sample of quasar pairs in HP06. Pairs that contain an absorber with column density $\text{Log } N_{\text{HI}} > 17.2$ are colored red while pairs that contain an absorber with column density $\text{Log } N_{\text{HI}} > 19.0$ are colored green. We have indicated the mean of the observed luminosities with a black line and the luminosities of the central black hole from our simulations in dashed blue lines. The vertical cyan lines indicate the bins used to calculate a set of mock lines of sight with the same distribution in impact parameter as the observations.

which cluster around luminous point sources and those underdense systems that just happen to be near sources. In addition it is crucial that these sorts of models be constructed to interpret quasar pair observations such as those in HP06.

We find that the results of our ray tracing algorithm SPHRAY cannot be reproduced with simple semi analytic models in which gas above a given density threshold is completely shielded from ionizing radiation. This is because the photoionization rate at any given point is determined by the partial shielding provided by the local density field and to a lesser degree the partial shadowing seen in Figure 11.

We have shown in Figure 9 that our GADGET + SPHRAY models naturally reproduce the observed shape of the N_{HI} column density distribution. We have also shown that the flattening feature around $\text{Log } N_{\text{HI}} = 20$ attributed to self shielding in the analytic work of Zheng & Miralda-Escudé (2002) is not due entirely to self shielding, but is largely enhanced by it.

When compared to the observations of HP06, our ray tracing and semi analytic models fall short of capturing the number of dense absorbers proximate to luminous quasars. We have described improvements to our model that would bring our results into agreement with these observations including sampling more massive host halos, correcting for the under resolved clumping of gas, allowing obscuration / periodic emission of the quasar radiation and using a larger simulation volume to better model uncertain radial separations. These issues are not intractable and can be dealt with using a larger low resolution simulation to sample more mas-

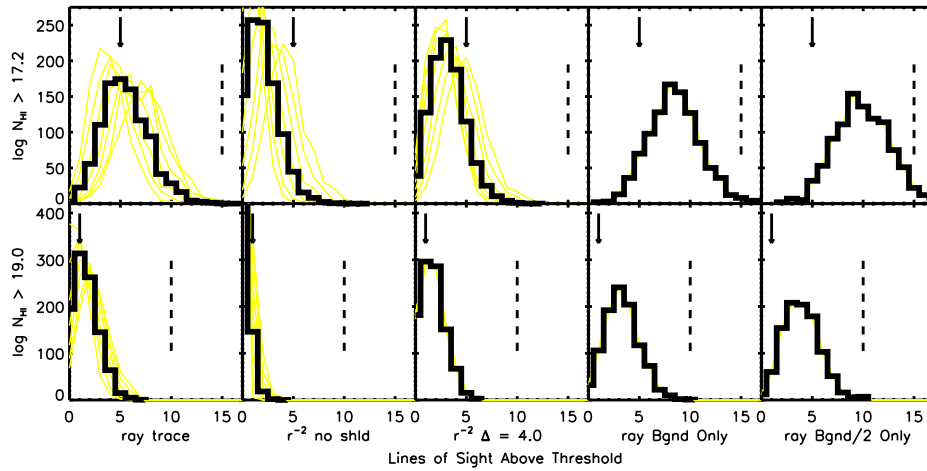


Figure 13. Lines of sight with column densities N_{HI} above $N_{\text{HI}}^{\text{th}}$ for several radiative models. We construct $N_{\text{mock}} = 1000$ groups of $N_{\text{los}} = 61$ lines of sight that match the impact parameter distribution of the HP06 sample. For the fiducial ray tracing model, we count the number of lines of sight above threshold in each of the N_{mock} groups and histogram the values. We repeat this procedure for each of the seven simulated quasar luminosities (see Figure 12) and plot the results as thin yellow lines in the upper left ($\text{Log } N_{\text{HI}}^{\text{th}} = 17.2$) and lower left ($\text{Log } N_{\text{HI}}^{\text{th}} = 19.0$) panels. Overlaid on these lines in thick black is the luminosity weighted average of each bin. The weighting is done by determining the fraction of HP06 quasars that is nearest to each simulated quasar luminosity. In the second and third columns we repeat this procedure for two semi analytic models. The last two columns show the same thing for ray tracing runs that include only a UV background sent in from outside the box (fiducial in fourth column and half the fiducial in fifth column). These are useful in describing the effects of beaming. We have indicated the observed values from HP06 (vertical dashed lines) and the peak of the luminosity weighted average from the fiducial ray tracing runs (arrow) in each panel.

sive dark matter host halos coupled with a high resolution resimulation of a more representative proximity zone.

Finally we have shown that the total amount of neutral HI within the $750 h^{-1}$ kpc region around our central quasar can change by up to an order of magnitude depending on the shielding prescription used. This means that HI surveys that do not resolve individual galaxy features but whose goal is to measure the integrated signal from a proximity zone will need to take these effects into account. This is on scales much smaller than the intensity mapping proposed by Peterson et al. (2009) to measure Baryon Acoustic Oscillations, but would be relevant for connecting HI or 21 cm galaxy surveys to the underlying density field.

ACKNOWLEDGMENTS

We would like to thank Joseph Hennawi and Xavier Prochaska for reading an early version of this manuscript and offering many useful suggestions. We would also like to thank the Intel Corporation, the Moore Foundation, and Bruce and Astrid McWilliams for the provision of large scale computing resources necessary to complete this work. This work was also supported by the NASA Astrophysics Theory Program, contract NNG 06-GH88G, and NSF grants AST-0507665 and OCI-0749212.

APPENDIX A: RADIATIVE TRANSFER CONVERGENCE

Here we examine the convergence of our ray tracing radiative transfer runs. In these runs, both the photoionization rate Γ_{HI} and the neutral fractions x_{HI} are taken as outputs from SPHRA. In Figure A1 we show the evolution of x_{HI} as the number of rays traced is increased over four decades. The distribution has a triple peaked structure with the left peak being due mostly to collisional ionizations, the central peak due mostly to photoionizations in the diffuse IGM and the right peak formed by self shielded particles. The photoionization peak has not converged completely however there is a very small amount of neutral material here and our main interest is in the self shielded peak which has very nearly reached convergence.

In Figure A2 we examine the convergence of Γ_{HI} . For studying self shielding, the position of the peak is not as important as the tail of the distribution extending to smaller photoionization rates. The slightly smaller values in the tail for the rt9 run translate into slightly less neutral material with $-3 < x_{\text{HI}} < -1$.

REFERENCES

- Altay G., Croft R. A. C., Pelupessy I., 2008, MNRAS, 386, 1931
- Antonucci R., 1993, ARA&A, 31, 473
- Bagla J. S., 2002, JApA, 23, 185
- Bajtlik S., Duncan R. C., Ostriker J. P., 1988, ApJ, 327, 570

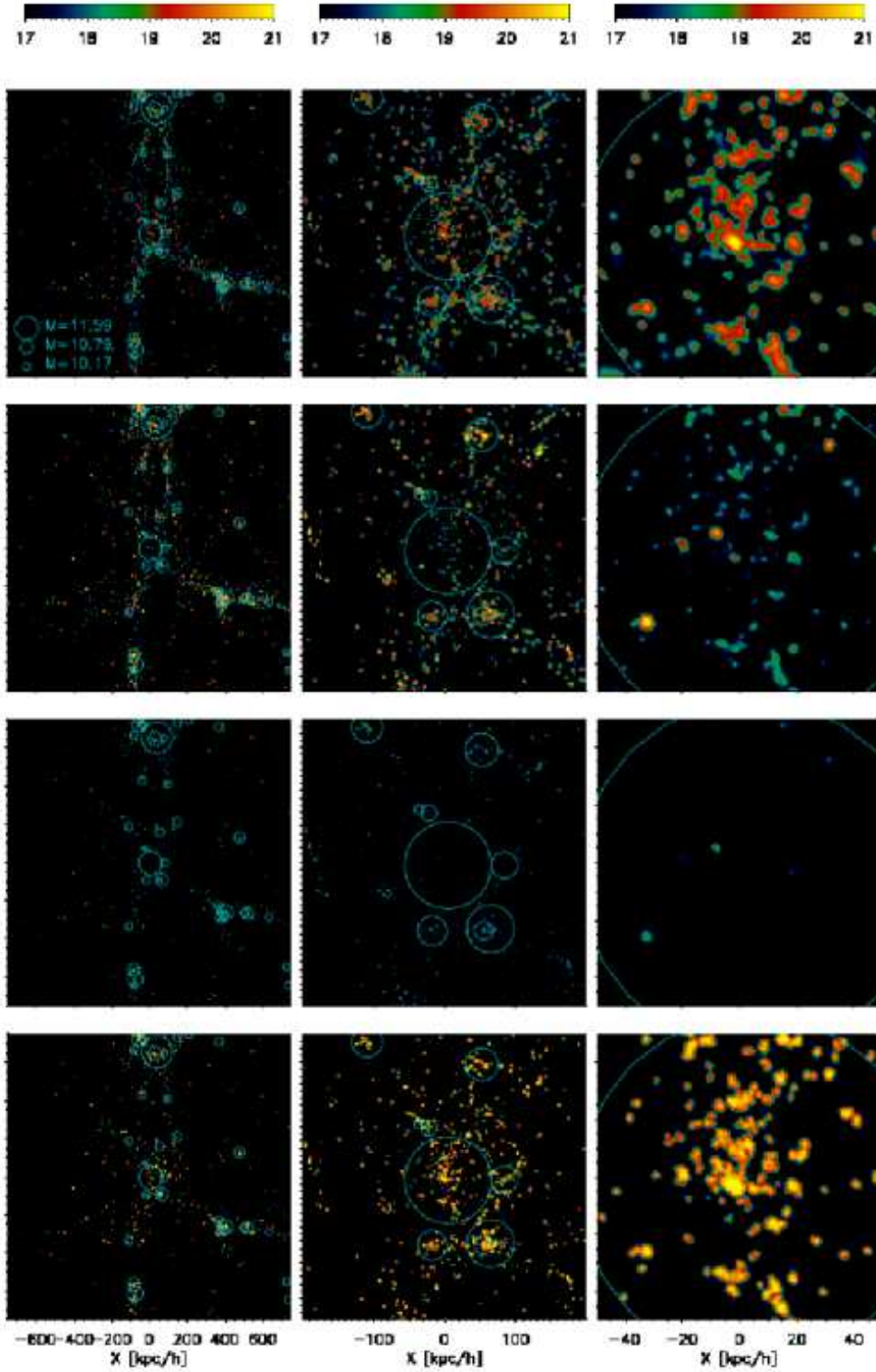


Figure 14. The HI column density obtained by collapsing the 1500 kpc/h simulation volume along the z-axis. The top row shows the direct GADGET output with no central UV field from the quasar, the top middle row shows the GADGET + SPHRA model, the bottom middle row shows the semi analytic model with no shielding, and the bottom row shows a semi analytic model with a shielding threshold at $\Delta = 4.0$. The central quasar has the same luminosity in all three models which include it. Overlaid in solid cyan lines are the galaxies that were identified in the parent hydrodynamic simulation. The radius of each circle is proportional to the cube root of the gas mass. We have indicated $\text{Log } M[M_{\odot}/h]$ for three galaxies chosen to be representative of the spread in mass. The symbol with $\text{Log } M = 11.59$ is the central quasar host galaxy.

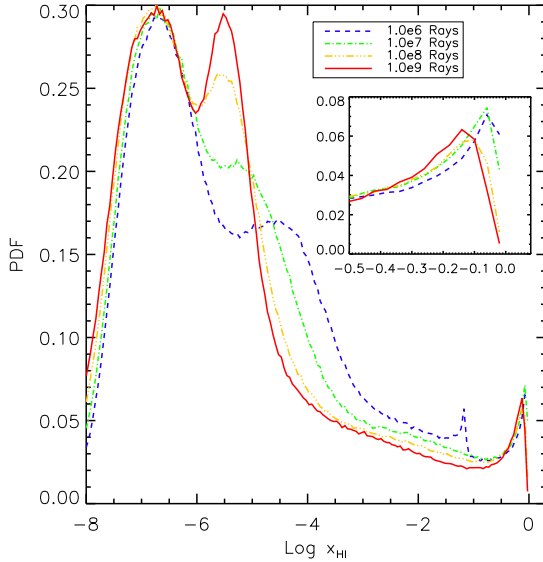


Figure A1. Mass weighted probability distribution of x_{HI} for the fiducial GADGET + SPHRAy ray tracing model including the background and the central quasar with varying numbers of rays traced. Shown as an inset is a close up of the self shielding neutral peak.

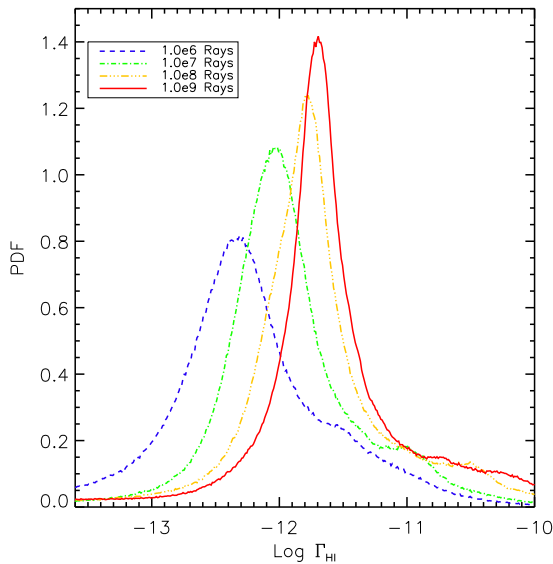


Figure A2. Mass weighted probability distribution of Γ_{HI} for the fiducial GADGET + SPHRAy ray tracing model including the background and the central quasar with varying numbers of rays traced. Shown as an inset is a close up of the self shielding neutral peak.

Cen R., Ostriker J. P., Prochaska J. X., Wolfe A. M., 2003, *ApJ*, 598, 741
 Coil A. L., Hennawi J. F., Newman J. A., Cooper M. C., Davis M., 2007, *ApJ*, 654, 115
 Croft R. A. C., 2004, *ApJ*, 610, 642
 Croom S. M., Boyle B. J., Shanks T., et al., 2005, *MNRAS*, 356, 415

DeGraf C., Di Matteo T., Springel V., 2009, ArXiv e-prints 0910.1843
 Di Matteo T., Colberg J., Springel V., Hernquist L., Sijacki D., 2008, *ApJ*, 676, 33
 Di Matteo T., Springel V., Hernquist L., 2005, *Nature*, 433, 604
 Faucher-Giguère C.-A., Lidz A., Hernquist L., Zaldarriaga M., 2008, *ApJ*, 688, 85
 Gardner J. P., Katz N., Hernquist L., Weinberg D. H., 1997a, *ApJ*, 484, 31
 Gardner J. P., Katz N., Hernquist L., Weinberg D. H., 2001, *ApJ*, 559, 131
 Gardner J. P., Katz N., Weinberg D. H., Hernquist L., 1997b, *ApJ*, 486, 42
 Haardt F., Madau P., 1996, *ApJ*, 461, 20
 Haehnelt M. G., Steinmetz M., Rauch M., 1998, *ApJ*, 495, 647
 Hennawi J. F., Prochaska J. X., 2007, *ApJ*, 655, 735
 Hennawi J. F., Prochaska J. X., Burles S., et al., 2006, *ApJ*, 651, 61
 Katz N., Weinberg D. H., Hernquist L., 1996a, *ApJS*, 105, 19
 Katz N., Weinberg D. H., Hernquist L., Miralda-Escudé J., 1996b, *ApJL*, 457, L57+
 Kim Y.-R., Croft R. A. C., 2008, *MNRAS*, 387, 377
 Marconi A., Risaliti G., Gilli R., Hunt L. K., Maiolino R., Salvati M., 2004, *MNRAS*, 351, 169
 Martini P., Weinberg D. H., 2001, *ApJ*, 547, 12
 Miralda-Escudé J., 2005, *ApJL*, 620, L91
 Nagamine K., Wolfe A. M., Hernquist L., Springel V., 2007, *ApJ*, 660, 945
 Peterson J. B., Aleksan R., Ansari R., et al., 2009, ArXiv e-prints 0902.3091
 Pontzen A., Governato F., Pettini M., et al., 2008, *MNRAS*, 390, 1349
 Porciani C., Magliocchetti M., Norberg P., 2004, *MNRAS*, 355, 1010
 Prochaska J. X., Hennawi J. F., 2009, *ApJ*, 690, 1558
 Rauch M., 1998, *ARA&A*, 36, 267
 Razoumov A., Cardall C., 2005, *MNRAS*, 362, 1413
 Razoumov A. O., Norman M. L., Prochaska J. X., Wolfe A. M., 2006, *ApJ*, 645, 55
 Schaye J., 2006, *ApJ*, 643, 59
 Schirber M., Bullock J. S., 2003, *ApJ*, 584, 110
 Scott J., Bechtold J., Dobrzycki A., Kulkarni V. P., 2000, *ApJS*, 130, 67
 Shakura N. I., Syunyaev R. A., 1973, *A&A*, 24, 337
 Shen Y., Strauss M. A., Oguri M., et al., 2007, *AJ*, 133, 2222
 Shen Y., Strauss M. A., Ross N. P., et al., 2009, *ApJ*, 697, 1656
 Spergel D. N., Verde L., Peiris H. V., et al., 2003, *ApJS*, 148, 175
 Springel V., 2005, *MNRAS*, 364, 1105
 Springel V., Di Matteo T., Hernquist L., 2005, *MNRAS*, 361, 776
 Springel V., Hernquist L., 2002, *MNRAS*, 333, 649
 Springel V., Hernquist L., 2003, *MNRAS*, 339, 289
 Weinberg D. H., Davé R., Katz N., Kollmeier J. A., 2003, in *The Emergence of Cosmic Structure*, edited by S. H. Holt, C. S. Reynolds, vol. 666 of *American Institute of Physics Conference Series*, 157–169

Wolfe A. M., Gawiser E., Prochaska J. X., 2005, ARA&A,
43, 861

Zheng Z., Miralda-Escudé J., 2002, ApJL, 568, L71